PAPER

Check for updates

Reversible control of magnetism: on the conversion of hydrated FeF₃ with Li to Fe and LiF†

Ruby Singh,[ab] Ralf Witte,[a] Xiaoke Mu,[a] Torsten Brezesinski, [iD][a] Horst Hahn,[ab] Robert Kruk[a] and Ben Breitung [iD] *[ac]

Conversion-type electrode materials are prominent examples of potential Li-ion battery cathodes and/or anodes with large specific capacities. Conversion reactions often rely on complete reduction or oxidation of a transition metal, leading to multi-electron redox processes per formula unit, accompanied by changes of crystal structure and electronic configuration and, consequently, of materials properties such as magnetization. Here, we report on the utilization of the FeF₃/Fe conversion reaction to reversibly control the magnetization. Hydrated FeF₃ was chosen as electrode material and the changes in magnetization upon reversible redox reaction against Li counter electrode monitored by means of Superconducting Quantum Interference Device magnetometry. *In situ* measurements provide insights into the changes in magnetization occurring during the conversion reaction, specifically revealing the transition from paramagnetism to ferromagnetism.

1. Introduction

Materials with tailorable and tunable properties are receiving great interest in materials science. The possibility to tailor or tune properties is a desired feature for the development of functional materials for various applications. While tailoring means generating a specific structure or architecture of the material to achieve a certain property, the tuning concept addresses reversible changes of properties by means of an external control parameter. One possibility to reversibly change the characteristics of a material is to vary the magnetic interactions between electrons, thus leading to different types of magnetic responses in a magnetic field. This concept of magnetization tuning has been shown by, *e.g.*, magnetoelectric coupling at ferromagnetic/ferroelectric interfaces.[1–8] Additionally, electron- or hole-doping has been shown to modify the type of magnetism in $La_{1-x}Sr_xMnO_3$ (LSMO); doping can be achieved either by altering the elemental composition of LSMO (additional Sr leads to hole doping, resulting in a tailored structure) or by applying an electric field, which reversibly changes the carrier concentration in LSMO.[9–14]

[a]Institute of Nanotechnology, Karlsruhe Institute of Technology (KIT), Hermann-von-Helmholtz-Platz 1, 76344 Eggenstein-Leopoldshafen, Germany

[b]Joint Research Laboratory Nanomaterials, Technische Universität Darmstadt & Karlsruhe Institute of Technology (KIT), Otto-Berndt-Str. 3, 64287 Darmstadt, Germany

[c]Karlsruhe Nano-Micro Facility (KNMF), Karlsruhe Institute of Technology (KIT), Hermann-von-Helmholtz-Platz 1, 76344 Eggenstein-Leopoldshafen, Germany

† Electronic supplementary information (ESI) available. See DOI: 10.1039/c9ta08928d

However, the tuning of LSMO using an external electric field constitutes only a surface effect depending on the affected magnetic depth.[15] In order to address the bulk material, a different concept has been applied recently.[16–19] For example, the magnetization of bulk γ-Fe₂O₃ could be tuned by reversible intercalation of Li⁺ into vacant sites of the lattice structure.[20,21] This idea is derived from the concept of Li-ion batteries (LIBs), where active materials are reversibly de/lithiated over thousands of cycles and show distinct redox reactions depending on the applied potential. These redox reactions are often accompanied by changes in magnetization due to the transferred electrons. The most common electrode materials for LIBs are intercalation materials,[22–26] where lithium is intercalated into a host structure but does not extensively change the crystal structure of the active material. Usually, only a fraction of the redox active ions in the active material is being reduced or oxidized (*e.g.*, $LiCo^{(III)}O_2/Co^{(IV)}O_2$) to prevent material degradation due to changes in crystal structure. In contrast to intercalation materials, conversion materials are based on complete structural conversion. The reduction of, *e.g.*, $Fe^{(III)}F_3$ to $Fe^{(0)}$ requires three electrons per formula unit and completely rebuilds the material. In the latter case, the conversion is accompanied by a transition of antiferromagnetic FeF₃ to ferromagnetic Fe. Many different metal fluoride compounds are reported to be LIB cathode alternatives with high specific capacity but low reversibility resulting from the complex conversion reactions.[27–30]
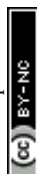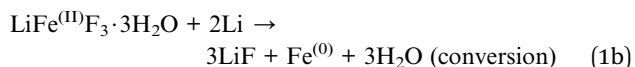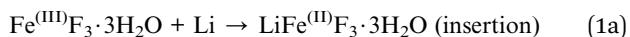
In the present work, the concept of *in situ* monitoring the lithiation of an electrochemically active material is extended from the intercalation approach to the reversible conversion reaction of FeF₃·3H₂O (β-FeF₃) (eqn (1)). The conversion of

This journal is © The Royal Society of Chemistry 2019

J. Mater. Chem. A, 2019, **7**, 24005–24011 | 24005

$FeF_3 \cdot 3H_2O$ to Fe delivers a specific capacity of 712 mA h g^{-1} owing to the three electron reduction.[31–33] The conversion mechanism is a two-step process, comprising an insertion and a subsequent conversion reaction step.[34,35]

$$Fe^{(III)}F_3 \cdot 3H_2O + Li \rightarrow LiFe^{(II)}F_3 \cdot 3H_2O \text{ (insertion)} \quad (1a)$$

$$LiFe^{(II)}F_3 \cdot 3H_2O + 2Li \rightarrow$$
$$3LiF + Fe^{(0)} + 3H_2O \text{ (conversion)} \quad (1b)$$

These measurements were performed by coupling Superconducting Quantum Interference Device (SQUID) magnetometry with cyclic voltammetry (CV) measurements. A customized electrochemical cell using an ionic liquid as electrolyte was built to adapt to the conditions of the SQUID. The changes in magnetization during the reversible FeF_3/Fe conversion were tracked and the features assigned to the respective increase and decrease of current during cycling operation. The magnetic data are supported by TEM, EELS and Mössbauer spectroscopy. Apart from the complete conversion, the insertion of Li into the $FeF_3 \cdot 3H_2O$ host structure has been studied as well.

2. Results and discussion

The changes in magnetization during the conversion reaction were monitored using combined CV/SQUID measurements. FeF_3 and $FeF_3 \cdot 3H_2O$ are known conversion materials and subject of many studies (for application as potential cathodes in LIBs).[36–40] The electrodes for the measurements were prepared using polyvinyl alcohol (PVA) as binder, since it is known to form a flexible polymer network. PVA is often used for conversion and alloying electrodes, as it can withstand volume expansions during the redox reactions. PVA is prepared as aqueous solution, therefore we chose the most hydrated FeF_3 form as starting material to prevent changes during slurry preparation. Commercial $FeF_3 \cdot 3H_2O$ material was analyzed using Mössbauer spectroscopy and contains around 97% $FeF_3 \cdot 3H_2O$ and 3% FeF_3 (Table 1).

The sample for combined CV/SQUID measurements was prepared in a customized electrochemical cell using a mixture of $FeF_3 \cdot 3H_2O$, conductive carbon black and PVA binder as electrode and Li foil as counter electrode. A detailed description of the slurry preparation can be found in the Experimental section. The measurement setup and cell used are described in more detail in Fig. S1.† CV measurements were performed while measuring the changes in magnetization at an applied field of 0.1 T. A considerably weak magnetic field was used to prevent

side reactions that appeared when stronger fields were applied, most probably due to $Fe^{(0)}$ particles responding to the field and penetrating the separator, leading to short circuits. The redox reactions of $FeF_3 \cdot 3H_2O$ upon lithiation have been described in the literature (eqn (1)) and comprise insertion of Li into FeF_3 and subsequent conversion to Fe.[41] While the insertion reaction is reported to be reversible, the conversion reaction leads to accelerated degradation.[42] These two mechanisms were independently monitored and Fig. 1 shows the evolution of the magnetic moment with cycling in the insertion regime between 2 and 4.5 V vs. Li$^+$/Li.

The insertion is described to be reversible, since, in contrast to a conversion reaction, the crystal structure undergoes minor changes.[43] Therefore, the respective insertion reaction of $FeF_3 \cdot 3H_2O$ to $LiFeF_3 \cdot 3H_2O$ only results in a slight rearrangement of the structure.[43] As discussed, the sample represents a mixture of about 3% FeF_3 and 97% $FeF_3 \cdot 3H_2O$, thus the changes in magnetic moment can be attributed to either of these species. FeF_3 is known to exhibit antiferromagnetism at room temperature, whereas the zero-field-cooled/field-cooled (ZFC/FC) curves for $FeF_3 \cdot 3H_2O$ reveal a Néel temperature at around 140 K (Fig. S3†). Below this temperature, some antiferromagnetic orientations of spins are apparent (1-dimensional antiferromagnetism along the chains) and the behavior increases with decreasing temperature as the chains begin to couple.[44] Density functional theory (DFT) calculations by Zheng et al. indicate an alternating change of the ground state magnetization between antiferromagnetism and ferrimagnetism depending on the lithiation level of FeF_3.[43] While $LiFeF_3$, $Li_{0.5}FeF_3$ and FeF_3 were found to be antiferromagnetic in nature, both $Li_{0.75}FeF_3$ and $Li_{0.25}FeF_3$ appear to show ferrimagnetic behavior. In our data, which were recorded at room temperature, we see a similar behavior, i.e., an alternating increase and decrease of magnetization depending on the lithiation degree. The insertion reactions seem to involve several steps, which are repeatedly changing the magnetization of the sample. The current progression and the respective changes in magnetization appear to be very reversible, therefore we conclude that the redox reactions do not result in major changes of the crystal structure (note that this would lead to material degradation). The magnetization after one complete cycle does not coincide with the magnetization before cycling; in fact, an increased value is found after each cycle. The increase is noticed in every cycle and may be the reason for the continuous growth of magnetization background with cycling operation. A possible explanation might be the slight change of structure when

Table 1 Mössbauer hyperfine parameters resulting from the fit to the data. The asterisk denotes a fixed fit parameter

Sample		IS (mm s^{-1})	QS (mm s^{-1})	B_{HF} (T)	Γ (mm s^{-1})	Area (%)
Pristine	$Fe^{(III)}$ doublet	0.432	0.63	—	0.27	97
	$Fe^{(III)}$ sextet	0.47	0.003	39.8	0.40	3
Discharged	$Fe^{(III)}$	0.47	0.54	—	0.47	23
	$Fe^{(II)}$	1.220	1.73	—	0.85	53
	$Fe^{(0)}$	0*	—	—	0.6	24

24006 | J. Mater. Chem. A, 2019, 7, 24005–24011

This journal is © The Royal Society of Chemistry 2019

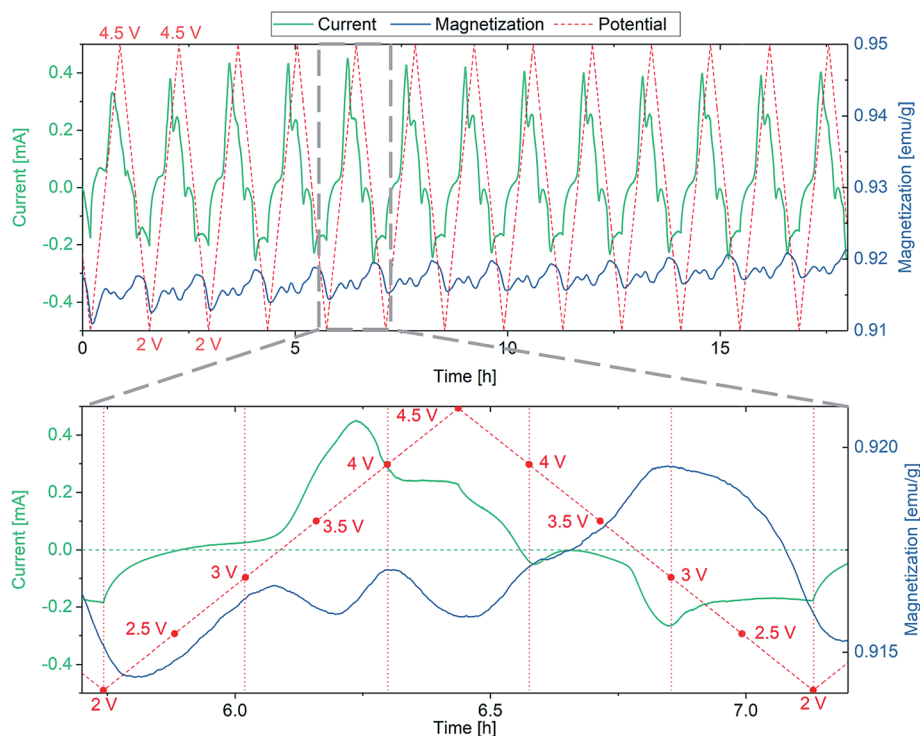**Fig. 1** First 13 cycles of the $FeF_3 \cdot 3H_2O$/Li insertion reaction (top) with a more detailed view of the 5th cycle (bottom). CV/SQUID measurements showing the evolution of magnetization with current and potential. The sweep rate was 1 mV s^{-1}. The horizontal dashed green line in the bottom panel represents the zero line of current, while the vertical red dotted lines denote the potential at the respective time. Corresponding cyclic voltammograms can be found in the ESI (Fig. S2†).

achieving a lithiation level of $x > 0.5$ in Li_xFeF_3, which apparently is not fully reversible. Yamakawa *et al.* reported a pronounced change in XRD pattern upon insertion of >0.5 Li in FeF_3, resulting from the conversion of the FeF_3 crystal structure (ReO_3-type).[45] Moreover, Doe *et al.* describe a possible precipitation of nanosized Fe when $x > 0.5$ (in Li_xFeF_3), which may be the reason for the irreversible increase in magnetization.[33,45] We assume that a combination of structural and electronic processes, appearing during the insertion processes, lead to the described increase in magnetization. Nevertheless, the clear reason for this result remains unclear at present.

Similar measurements have been performed between 1 and 4.5 V (*vs.* Li$^+$/Li) to include the conversion reaction of $FeF_3 \cdot 3H_2O$ (eqn (1)). Fig. 2 shows the dependence of magnetization on the redox reactions occurring during this conversion, the change in magnetization being around 1000 times larger compared to the insertion regime. This is a clear indication for the conversion of the paramagnetic material to a ferromagnetic one.

As explained above, the overall reversibility of the $FeF_3 \cdot 3H_2O$ conversion reaction is reported to be relatively low due to structural changes. The magnetization changes during conversion are superimposing the weak insertion variations. The
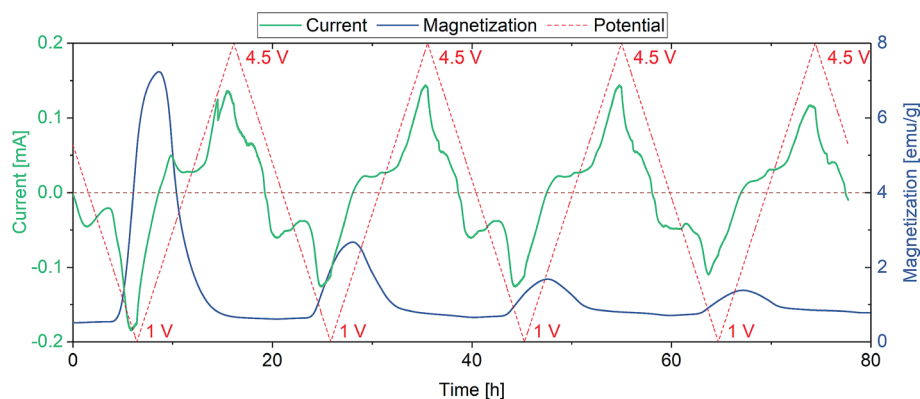

Fig. 2 Conversion reaction of $FeF_3 \cdot 3H_2O$. The sweep rate was set to 0.1 mV s^{-1} to account for the slow kinetics of conversion reactions in general. Magnetization degradation with cycling is observed, reflecting the decreasing appearance of Fe$^{(0)}$.

This journal is © The Royal Society of Chemistry 2019

J. Mater. Chem. A, 2019, **7**, 24005–24011 | **24007**

curves in Fig. 2 can be explained as follows: upon lithiation, $FeF_3 \cdot 3H_2O$ converts to Fe and LiF. The reduction reaction can be tracked by the increase in absolute current (green line, negative current values) and results in an increase in magnetization below the FeF_3/Fe redox potential. The magnetization reaches its maximum when the potential is not sufficient anymore to reduce more FeF_3 to Fe. With increasing potential, the current increases and when it becomes positive the reverse reaction (Fe + 3LiF → FeF_3 + 3Li) takes place. This is accompanied by a decrease in magnetization. The highest slope of the magnetization increase is coinciding with the lowest potential, indicating the proceeding conversion reaction. The decreasing intensity of the magnetization change with cycling is related to the irreversibility of the conversion reaction. It appears that with every cycle less $FeF_3 \cdot 3H_2O$ can be converted to Fe, and therefore, the specific capacity decreases. This behavior is reflected as well by the current, showing decreasing values at low potential during cycling. This partial irreversibility of the FeF_3 conversion reaction has been reported in several studies.[35,36,46] Additionally, stepwise background increase of magnetization after each conversion reaction is observable. This indicates the presence of particles that remain in a ferri- or ferromagnetic state and do not participate in the reaction anymore. To further evaluate the magnetization, magnetization curves were recorded. The evolution of magnetization with increasing magnetic field is shown in Fig. 3, where the as-prepared material, the electrode at different lithiation states (2 V for insertion, 1 V for conversion) and at the higher cutoff potential (4.5 V) are compared with the empty electrochemical tuning cell.

The magnetization curves were measured to exclude a possible contribution of the electrochemical cell housing plus all integral parts such as wires, seals and connections to the measurement devices. Hereby, the as-prepared sample (yellow line) will first be lithiated (green curve, 2 V, insertion) and converted to the fully discharged state (blue curve, 1 V, conversion) with a subsequent delithiation to the charged state at 4.5 V (red curve). The brown line indicates that there is no

significant contribution of the housing to the magnetization. The as-prepared material shows paramagnetic behavior, while the fully discharged (Fe + LiF) and fully charged (FeF_3) states indicate cooperative effects, presumably ferromagnetic coupling. Note that the fully delithiated species can be also described as Li_yFeF_x, as many indications appear in the literature that FeF_3 cannot be completely regained.[33,41] Nevertheless, the weak ferromagnetic behavior is not expected in the fully charged state of the material. As mentioned, the evolution of magnetization in the CV/SQUID measurements shows a continuous increase in background with increasing cycle number. This may suggest that not every Fe particle formed during the lithiation process of the conversion reaction can be converted back during the delithiation process. These remaining Fe particles would show a ferromagnetic signature. Thus, the shape of curve for the fully charged sample likely results from an overlap of the ferromagnetic state of the remaining Fe particles and the state of the delithiated material.

Quantification of the Fe species ($Fe^{(0)}$, $Fe^{(II)}$, $Fe^{(III)}$) present in the as-prepared and the fully lithiated species was performed using Mössbauer spectroscopy. Additionally, the magnetic states were investigated. The as-prepared sample shows a spectrum, which can be well represented with a doublet, with isomer shift (IS) of $FeF_3 \cdot 3H_2O$ (β-FeF_3) and quadrupole splitting (QS) characteristic of $Fe^{(III)}$, being in good agreement with the literature (Fig. 4).[47] An additional component with magnetic sextet can be attributed to antiferromagnetic FeF_3, with a magnetic hyperfine field B_{HF} of about 40 T. Table 1 summarizes the fitting results.[48]

In contrast, the discharged sample features a drastically altered spectrum, as expected based on the results of the changes observed in the magnetic properties during the electrochemical reduction process. The spectrum can be represented using three sub-spectra. A minor component with an IS and a QS typical of $Fe^{(III)}$, which is very similar to the pristine material, a distinctly split $Fe^{(II)}$ component and a singlet-like component with an IS being very close to what is expected
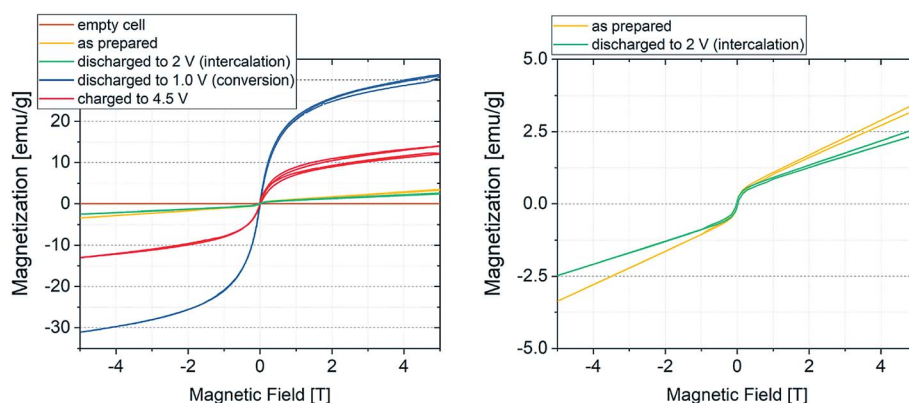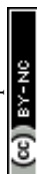

Fig. 3 Room temperature magnetization curves of the sample at different potentials. The brown line represents the empty electrochemical tuning cell, while the blue and red curves display the magnetization of the material in its fully discharged (Fe + LiF) and fully charged (FeF_3) state, respectively. The green curve denotes the material discharged to 2 V (insertion regime) and the yellow curve the as-prepared material. The cure splitting results from self-discharge during the measurement. Since the sample is not completely in equilibrium state, the open circuit potential slightly changes over time. This indicates that even small state of charge changes can be detected using coupled CV/SQUID measurements.
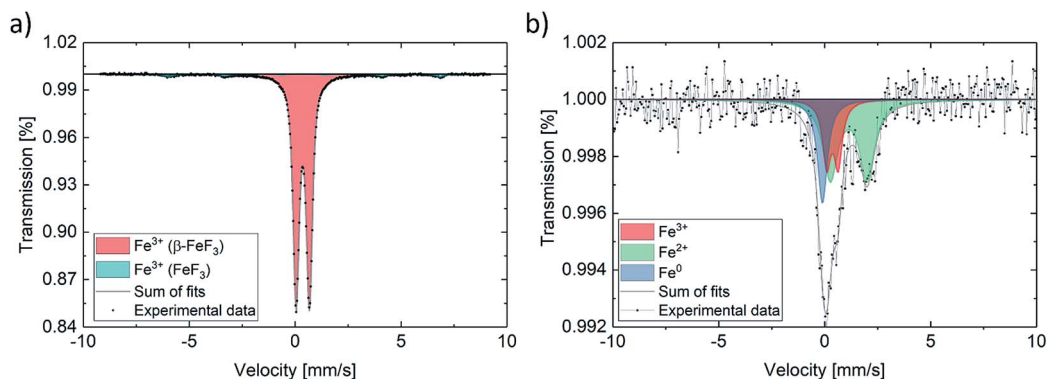
24008 | J. Mater. Chem. A, 2019, 7, 24005–24011

This journal is © The Royal Society of Chemistry 2019

Fig. 4 Mössbauer spectrum for (a) as-prepared powder and (b) fully lithiated material (initial discharge).

for metallic Fe. The fit is a bit ambiguous due to the strong overlap of the sub-spectra, however, with additional evidence from TEM (next paragraph), it is reasonable to attribute the singlet component to reduced $Fe^{(0)}$. $Fe^{(0)}$ is present in a nanoparticulate form and therefore shows a singlet, characteristic of the superparamagnetic state. The latter interpretation is in agreement with the magnetometry data, which do not show the full magnetic moment of $Fe^{(0)}$. This can be well understood by the fact that the magnetization of Fe nanoparticles may not be fully saturated in the accessible magnetic field. The spectrum and its interpretation correspond well with what has been found by *ex situ* and *operando* Mössbauer experiments on a similar electrochemical cell.[29,49] The quantification of Fe species in the discharged sample further shows that only some of the $FeF_x \cdot 3H_2O$ can be converted to $Fe^{(0)}$ by using these measurement parameters. These results support the finding by other groups, describing the formation of differently structured FeF_3 and Li_xFeF_3 species instead of full conversion reaction to $Fe^{(0)}$ and FeF_3.[33] The magnetization further indicates that less of ferromagnetic $Fe^{(0)}$ is formed with increasing cycle number, which helps explain the low overall magnetization.

The expected saturation magnetization of $Fe^{(0)}$ amounts to 217.6 emu g^{-1}.[50,51] When compared to the measured values in Fig. 3, this value is not achieved. The sample shows a saturation magnetization of about 30 emu g^{-1} at 5 T. This difference can be explained by two effects. From the results of the Mössbauer measurements, the conversion reaction seems not to be complete, the amount of formed $Fe^{(0)}$ is smaller than the theoretical quantity calculated for a full conversion. This would lead to a lower absolute saturation magnetization. The second effect is related to the small particle size of the formed $Fe^{(0)}$. It is known that conversion reactions result in very small crystalline or amorphous nanoparticles, with sizes often being in the nm range.[45] Particles of such small size typically only show a single magnetic domain and specific electron spin behavior, therefore they are superparamagnetic in nature. The superparamagnetic behavior has been described for $Fe^{(0)}$ nanoparticles of diameter around 10 nm.[52–54]

To analyze if the $Fe^{(0)}$ particles in the cycled sample have diameters in the lower nm region and therefore could show superparamagnetic behavior, TEM investigations have been performed. Fig. 5a shows a HAADF-STEM micrograph of the fully discharged sample, with the SAED indicating an fcc structure, most probably that of LiF (Fig. 5b).

To identify the elements, EELS has been conducted on the same area (Fig. 5c and d), revealing anticorrelation of the spatial distribution of Li (green) and Fe (red). The $Fe^{(0)}$ size has been determined by HR-TEM (Fig. 5e). In fact, particles having diameters between 5 and 10 nm and a bcc structure were found. Consequently, the size dependent transition from ferromagnetic to superparamagnetic state during the conversion reaction is a possible scenario and helps explain the magnetization in Fig. 3. For identification of Li and Fe, the Li–K and Fe–M edges located between 55 to 75 eV were used. These edges were chosen to prevent beam damage on beam sensitive LiF and to still obtain good signal-to-noise ratios. Because the F–K edge is located at 685 eV and the EELS signal reduces exponentially with higher energies, a 50 times higher dose is required to map the F in LiF. During our experiments, this led to severe beam damage on the LiF particles. Thus, we determined LiF and Fe *via* SAED and showed the anticorrelation of Li and Fe with EELS. Taken together, this demonstrates the presence of Fe and LiF in the discharged state of the electrode.

3. Experimental

Sample preparation

The $FeF_3 \cdot 3H_2O$/carbon C65 nanocomposite was obtained by ball-milling a $FeF_3 \cdot 3H_2O$ (Alfa Aesar)/carbon black (C65) (Timcal) mixture at 500 rpm for 3 h using a Retsch PM 100 planetary ball mill with WC vials and a ball-to-powder ratio of 20 : 1. Afterwards, the slurry was prepared by mixing the ball-milled sample with carbon C65 additive and an aqueous Selvol 425 PVA binder solution (70 : 20 : 10 weight ratio). The resulting slurry was pasted onto Cu foil (Gould Electronics) by doctor-blading and then dried in a vacuum oven at 80 °C for 12 h. The active material loading varied from 0.35 to 2 mg cm^{-2}, depending on the measurement type (M/H-curves, CV/SQUID measurements).
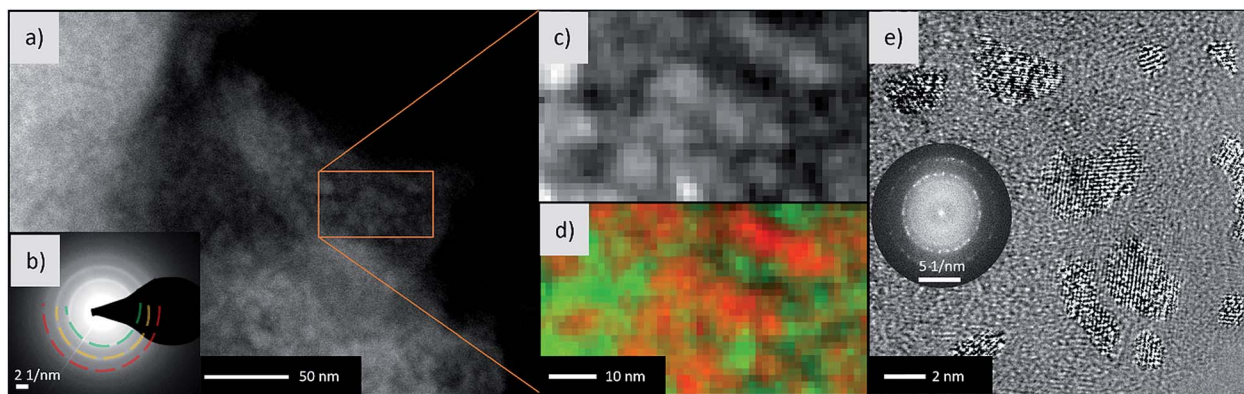
Fig. 5 Electron microscopy of the discharged material. (a) STEM-HAADF micrograph with (b) the SAED pattern of the lithiated sample. The broad ring of d-spacing 2.34 Å can be attributed to the (111) plane of LiF. (c) Enlarged micrograph of the area denoted by the rectangular box and (d) the corresponding elemental map for Li$^+$ (green) and Fe atoms (red) from EELS (Li–K and Fe–M edge). (e) HR-TEM micrograph and FFT of the shown crystallites (contrast enhanced to make the crystallites better visible).

Cell assembly

An electrochemical tuning cell (Fig. S1†) was used for combined CV/SQUID measurements. Therefore, the prepared electrode, glass fiber separator (GF/A, Whatman) and lithium foil (China Lithium Ltd) as counter electrode were stacked and assembled in the cell. LiTFSI (20 wt%, Sigma Aldrich) in EMIM-TFSI (Sigma Aldrich) was used as electrolyte to adapt to the SQUID measurement conditions (no organic solvent could be used, since accidental evaporation would lead to cell failure and contamination of the magnetometer).

Instrumentation

Potentiostatic measurements were performed using a µAutolab Type 3 (PGSTAT12/30/302) coupled with an MPMS3 SQUID with vibrating sample magnetometer (VSM). S/TEM was performed on a Titan 80-300 (FEI) operated at 300 kV equipped with imaging aberration (Cs) corrector and Gatan GIF Tridium 863 energy filter. ^{57}Fe Mössbauer spectra were recorded using a spectrometer in transmission geometry with a moving source of ^{57}Co in a Rh matrix and a triangular velocity variation. Care was taken to seal the sensitive samples into a plastic bag inside an argon-filled glove box to avoid oxidation. The isomer shift is given relative to bcc-Fe at room temperature.

4.   Conclusions

The impact of redox reactions on the magnetization during conversion of FeF$_3 \cdot$3H$_2$O to Fe has been successfully studied. While the insertion reaction is reversible, the conversion reaction is found to trigger severe degradation processes and irreversible reactions. The insertion reaction leads to different magnetic states of differently lithiated Li$_x$FeF$_3$ species. The conversion of paramagnetic FeF$_3 \cdot$3H$_2$O to ferromagnetic Fe$^{(0)}$, leading to major changes in magnetization, could be clearly tracked at low cell potentials. The saturation magnetization at larger magnetic fields can be explained by incomplete conversion reactions and by the small particle size (<10 nm), leading to

superparamagnetism. The presence of crystalline Fe$^{(0)}$ particles of diameter around 10 nm was observed by means of HR-TEM, SAED and EELS. Furthermore, Mössbauer spectroscopy confirmed the formation of superparamagnetic Fe$^{(0)}$ particles during the conversion reaction. These combined CV/SQUID measurements demonstrate that the reversibility issues, which have been reported for conversion-based FeF$_3 \cdot x$H$_2$O materials in electrochemical energy storage applications, also appear in the magnetic tuning experiments and can be analyzed in detail by monitoring the magnetization changes with cycling.

Conflicts of interest

There are no conflicts to declare.

Acknowledgements

References

1   P. M. Leufke, R. Kruk, R. A. Brand and H. Hahn, *Phys. Rev. B: Condens. Matter Mater. Phys.*, 2013, **87**, 1–9.
2   X. Chen, X. Zhu, W. Xiao, G. Liu, Y. P. Feng, J. Ding and R. W. Li, *ACS Nano*, 2015, **9**, 4210–4218.
3   G. Wei, L. Wei, D. Wang, Y. Tian, Y. Chen, S. Yan, L. Mei and J. Jiao, *RSC Adv.*, 2017, **7**, 2644–2649.
4   T. Yamada, K. Morita, K. Kume, H. Yoshikawa and K. Awaga, *J. Mater. Chem. C*, 2014, **2**, 5183–5188.
5   Y. Kasahara, T. Nishijima, T. Sato, Y. Takeuchi, J. Ye, H. Yuan, H. Shimotani and Y. Iwasa, *J. Phys. Soc. Jpn.*, 2011, **80**, 1–4.
6   J. Carvell, E. Ayieta, A. Gavrin, R. Cheng, V. R. Shah and P. Sokol, *J. Appl. Phys.*, 2010, **107**, 103913.

24010 | *J. Mater. Chem. A*, 2019, **7**, 24005–24011

This journal is © The Royal Society of Chemistry 2019

7 V. Sivakumar, S. Kumar, C. Ross and Y. Shao-Horn, *ECS Trans.*, 2007, **2**, 1–11.

8 N. A. Chernova, M. Ma, J. Xiao, M. S. Whittingham, J. Breger and C. P. Grey, *Chem. Mater.*, 2007, **19**, 4682–4693.

9 A. Molinari, P. M. Leufke, C. Reitz, S. Dasgupta, R. Witte, R. Kruk and H. Hahn, *Nat. Commun.*, 2017, **8**, 1–9.

10 C. Reitz, D. Wang, D. Stoeckel, A. Beck, T. Leichtweiss, H. Hahn and T. Brezesinski, *ACS Appl. Mater. Interfaces*, 2017, **9**, 22799–22807.

11 S. Dong, R. Yu, S. Yunoki, G. Alvarez, J. M. Liu and E. Dagotto, *Phys. Rev. B: Condens. Matter Mater. Phys.*, 2008, **78**, 1–4.

12 F. Matsukura, Y. Tokura and H. Ohno, *Nat. Nanotechnol.*, 2015, **10**, 209–220.

13 A. Rocher, O. Durand, J. Maurice, F. Pailloux, A. Barthe, R. Lyonnet and J. Contour, *Appl. Surf. Sci.*, 2002, **188**, 176–181.

14 X. Hong, A. Posadas, A. Lin and H. Ahn, *Phys. Rev. B: Condens. Matter Mater. Phys.*, 2003, **68**, 1–5.

15 A. Molinari, H. Hahn and R. Kruk, *Adv. Mater.*, 2018, 1703908.

16 C. Reitz, C. Suchomski, D. Wang, H. Hahn and T. Brezesinski, *J. Mater. Chem. C*, 2016, **4**, 8889–8896.

17 L. A. Dubraja, C. Reitz, L. Velasco, R. Witte, R. Kruk, H. Hahn and T. Brezesinski, *ACS Appl. Nano Mater.*, 2018, **1**, 65–72.

18 C. Navarro-Senent, A. Quintana, E. Menéndez, E. Pellicer and J. Sort, *APL Mater.*, 2019, **7**, 030701.

19 Q. Zhang, X. Luo, L. Wang, L. Zhang, B. Khalid, J. Gong and H. Wu, *Nano Lett.*, 2016, **16**, 583–587.

20 S. Dasgupta, B. Das, M. Knapp, R. A. Brand, H. Ehrenberg, R. Kruk and H. Hahn, *Adv. Mater.*, 2014, **26**, 4639–4644.

21 S. Dasgupta, B. Das, Q. Li, D. Wang, T. T. Baby, S. Indris, M. Knapp, H. Ehrenberg, K. Fink, R. Kruk and H. Hahn, *Adv. Funct. Mater.*, 2016, **26**, 7507–7515.

22 L. de Biasi, B. Schwarz, T. Brezesinski, P. Hartmann, J. Janek and H. Ehrenberg, *Adv. Mater.*, 2019, **31**, 1900985.

23 M. Bianchini, M. Roca-Ayats, P. Hartmann, T. Brezesinski and J. Janek, *Angew. Chem., Int. Ed.*, 2019, **58**, 10434–10458.

24 X. Lou, R. Li, X. Zhu, L. Luo, Y. Chen, C. Lin, H. Li and X. S. Zhao, *ACS Appl. Mater. Interfaces*, 2019, **11**, 6089–6096.

25 Q. Fu, R. Li, X. Zhu, G. Liang and L. Luo, *J. Mater. Chem. A*, 2019, 19862–19871.

26 X. Zhu, J. Xu, Y. Luo, Q. Fu, G. Liang, L. Luo, Y. Chen, C. Lin and X. S. Zhao, *J. Mater. Chem. A*, 2019, **7**, 6522–6532.

27 M. Nishijima, I. D. Gocheva, S. Okada, T. Doi, J. Ichi Yamaki and T. Nishida, *J. Power Sources*, 2009, **190**, 558–562.

28 F. Badway, N. Pereira, F. Cosandey and G. G. Amatucci, *J. Electrochem. Soc.*, 2003, **150**, A1209.

29 A. Pohl, M. Faraz, A. Schröder, M. Baunach, W. Schabel, A. Guda, V. Shapovalov, A. Soldatov, V. S. K. Chakravadhanula, C. Kübel, R. Witte, H. Hahn, T. Diemant, R. J. Behm, H. Emerich and M. Fichtner, *J. Power Sources*, 2016, **313**, 213–222.

30 X. Xu, S. Chen, M. Shui, L. Xu, W. Zheng, J. Shu, L. Cheng, L. Feng and Y. Ren, *Ionics*, 2015, **21**, 1003–1010.

31 T. Li, L. Li, Y. L. Cao, X. P. Ai and H. X. Yang, *J. Phys. Chem. C*, 2010, **114**, 3190–3195.

32 X. Fan, Y. Zhu, C. Luo, T. Gao, L. Suo, S. C. Liou, K. Xu and C. Wang, *J. Power Sources*, 2016, **307**, 435–442.

33 R. E. Doe, K. A. Persson, Y. S. Meng and G. Ceder, *Chem. Mater.*, 2008, **20**, 5274–5283.

34 Y. L. Shi, N. Wu, M. F. Shen, Y. L. Cui, L. Jiang, Y. H. Qiang and Q. C. Zhuang, *ChemElectroChem*, 2014, **1**, 645–654.

35 T. Takami, K. Matsui, H. Senoh, N. Taguchi, M. Shikano, H. Sakaebe and T. Fukunaga, *J. Alloys Compd.*, 2018, **769**, 539–544.

36 L. Liu, H. Guo, M. Zhou, Q. Wei, Z. Yang, H. Shu, X. Yang, J. Tan, Z. Yan and X. Wang, *J. Power Sources*, 2013, **238**, 501–515.

37 L. Li, F. Meng and S. Jin, *Nano Lett.*, 2012, **12**, 6030–6037.

38 G. Ali, J. Lee, W. Chang, B.-W. Cho, H.-G. Jung, K.-W. Nam and K. Y. Chung, *Sci. Rep.*, 2017, **7**, 42237.

39 B. Breitung, M. A. Reddy, V. S. K. Chakravadhanula, M. Engel, C. Kübel, A. K. Powell, H. Hahn and M. Fichtner, *Beilstein J. Nanotechnol.*, 2013, **4**, 705–713.

40 M. A. Reddy, B. Breitung, V. S. K. Chakravadhanula, C. Wall, M. Engel, C. Kübel, A. K. Powell, H. Hahn and M. Fichtner, *Adv. Energy Mater.*, 2013, **3**, 308–313.

41 F. Cosandey, J. F. Al-Sharab, F. Badway, G. G. Amatucci and P. Stadelmann, *Microsc. Microanal.*, 2007, **13**, 87–95.

42 J. Lee and B. Kang, *Chem. Commun.*, 2016, **52**, 9414–9417.

43 Y. Zheng, R.-F. Li, S.-Q. Wu, Y.-H. Wen, Z.-Z. Zhu and Y. Yang, *Electrochemistry*, 2013, **81**, 12–15.

44 G. Nénert, O. Fabelo, K. Forsberg, C. V. Colin and J. Rodríguez-Carvajal, *Dalton Trans.*, 2015, **44**, 14130–14138.

45 N. Yamakawa, M. Jiang, B. Key and C. P. Grey, *J. Am. Chem. Soc.*, 2009, **131**, 10525–10536.

46 D. L. Ma, Z. Y. Cao, H. G. Wang, X. L. Huang, L. M. Wang and X. B. Zhang, *Energy Environ. Sci.*, 2012, **5**, 8538–8542.

47 M. Burbano, M. Duttine, O. Borkiewicz, A. Wattiaux, A. Demourgues, M. Salanne, H. Groult and D. Dambournet, *Inorg. Chem.*, 2015, **54**, 9619–9625.

48 G. K. Wertheim, H. J. Guggenheim and D. N. E. Buchanan, *Phys. Rev.*, 1968, **169**, 465–470.

49 D. E. Conte, L. Di Carlo, M. T. Sougrati, B. Fraisse, L. Stievano and N. Pinna, *J. Phys. Chem. C*, 2016, **120**, 23933–23943.

50 A. J. McGrath, S. Cheong, A. M. Henning, J. J. Gooding and R. D. Tilley, *Chem. Commun.*, 2017, **53**, 11548–11551.

51 J. Crangle and G. M. Goodman, *Proc. R. Soc. A*, 2006, **321**, 477–491.

52 G. C. Papaefthymiou, *Nano Today*, 2009, **4**, 438–447.

53 R.-P. Methling, V. Senz, E.-D. Klinkenberg, T. Diederich, J. Tiggesbäumker, G. Holzhüter, J. Bansmann and K. H. Meiwes-Broer, *Eur. Phys. J. D*, 2001, **16**, 173–176.

54 D. Kumar, J. Narayan, A. Kvit, A. Sharma and J. Sankar, *J. Magn. Magn. Mater.*, 2001, **232**, 161–167.

This journal is © The Royal Society of Chemistry 2019

J. Mater. Chem. A, 2019, **7**, 24005–24011 | **24011**